JOURNAL OF GEOPHYSICAL RESEARCH, VOL. 108, NO. B1, 2060, doi:10.1029/2001JB000791, 2003

Constitutive properties for the shear failure of intact granite in seismogenic environments

Aitaro Kato,[1] Mitiyasu Ohnaka,[2] and Hiromine Mochizuki

Earthquake Prediction Research Center, Earthquake Research Institute, The University of Tokyo, Tokyo, Japan

Received 13 July 2001; revised 12 July 2002; accepted 6 September 2002; published 31 January 2003.

[1] To investigate how the parameters prescribing the slip-dependent constitutive law are affected by seismogenic environments, we conducted a series of triaxial fracture experiments using intact Tsukuba-granite samples, which were deformed at wet, temperature-pressure conditions that correspond to a crustal depth range down to 15 km at a strain rate of 10^{-5}/s. It is conclusively demonstrated that the critical slip displacement D_c is virtually constant at the conditions of depths shallower than 10 km, and that D_c increases with increasing depth at depths greater than 10 km, because of the effect of temperature in the brittle-plastic transition regime. The breakdown stress drop for intact rock is found to be roughly constant (100 MPa) in a depth range down to 15 km. The apparent fracture energy increases with increasing depth at depths greater than 10 km. These results consistently lead to the conclusion that the stability of the breakdown process is enhanced at depths greater than 10 km. *INDEX TERMS:* 5104 Physical Properties of Rocks: Fracture and flow; 7209 Seismology: Earthquake dynamics and mechanics; 7215 Seismology: Earthquake parameters; 8159 Tectonophysics: Evolution of the Earth: Rheology—crust and lithosphere; *KEYWORDS:* Constitutive law, shear fracture experiments, seismogenic environments, brittle-plastic transition regime, intact granite

Citation: Kato, A., M. Ohnaka, and H. Mochizuki, Constitutive properties for the shear failure of intact granite in seismogenic environments, *J. Geophys. Res.*, *108*(B1), 2060, doi:10.1029/2001JB000791, 2003.

1. Introduction

[2] The earthquake rupture at a shallow crustal depth is a shear failure instability occurring on a preexisting fault in lithospheric plates or on a plate boundary itself in terms of macroscopic view. There is, however, commanding evidence that the earthquake rupture process combines frictional slip failure on a preexisting fault with fracturing of intact rock. For instance, *Bouchon* [1997] analyzed four large earthquakes occurring along the San Andreas fault system and revealed that the breakdown stress drop $\Delta\tau_b$, defined as local stress drop in the breakdown zone behind the rupture front, varies greatly along the entire fault, and that $\Delta\tau_b$ at local patches of high slip on the fault ranges from 50 MPa to 100 MPa. Such high breakdown stress drops at local patches on the fault roughly equals the breakdown stress drop of intact rock. A local patch of high resistance to rupture growth on the fault, which may be what is called an "asperity" or a "barrier" [e.g., *Aki*, 1979; *Kanamori*, 1981], plays an important role in the recurrence of a large earthquake, and is a potential source of high-amplitude and high frequency seismic radiation.

[3] In addition, at crustal depths corresponding to the brittle-plastic transition regime, the frictional strength conforms to the shear fracture strength of intact rock, because the lithostatic pressure and temperature are high enough at those depths [*Ohnaka et al.*, 1997]. Since an earthquake rupture includes not only frictional slip failure but also the shear failure of intact rock, it is crucial to understand the shear fracture process of intact rock in terms of the governing law.

[4] To understand earthquake ruptures quantitatively, one must first establish the constitutive law that governs the breakdown process behind the propagating rupture front. Two constitutive formulations for earthquake ruptures have been made: the rate- and state-dependent formulation [e.g., *Dieterich*, 1978; *Ruina*, 1983] and the slip-dependent formulation [*Ida*, 1972; *Palmer and Rice*, 1973; *Ohnaka et al.*, 1987; *Matsu'ura et al.*, 1992]. In this paper, we adopt the slip-dependent constitutive law as the law governing earthquake ruptures, because the rate- and state-dependent constitutive law cannot quantitatively explain the shear fracture process of intact rock. Although *Sleep* [1999] extended the rate- and state-dependent law to unify the deformation theories for gouges with those for intact rock, no quantitative description of the shear fracture process of intact rock has yet appeared.

[5] Most of shallow earthquakes occur at depths ranging from the crustal surface down to 10–15 km, and large shallow earthquakes tend to rupture within this depth range. In such a seismogenic layer, ambient temperature ranges from room temperature up to 300–400°C, and both litho-

---

[1] Also at Institute for Frontier Research on Earth Evolution, Japan Marine Science and Technology Center, Yokosuka, Japan.

[2] Also at Department of Earth Sciences, University College London, London, UK.

0148-0227/03/2001JB000791$09.00

static pressure and pore pressure range from atmospheric pressure up to 300–400 MPa. Accordingly, the constitutive property of a fault zone may depend greatly on these ambient conditions in the seismogenic layer. Therefore, to describe the earthquake generation process quantitatively, we must know how ambient conditions affect the constitutive properties of the fault zone [e.g., *Ohnaka*, 1992; *Ohnaka et al.*, 1997; *Blanpied et al.*, 1995; *Lockner*, 1998].

[6] In view of problems mentioned above, we first of all need to know how the constitutive property of intact rock varies with depth in the seismogenic layer. However, only a few laboratory experiments [*Rummel et al.*, 1978; *Wong*, 1982; *Ohnaka et al.*, 1997; *Odedra et al.*, 2001] have attempted to evaluate constitutive properties for the rock fracture in seismogenic environments. We have therefore conducted a series of triaxial fracture experiments using intact granite under the temperature-pressure conditions that correspond to a crustal depth range down to 15 km.

2. Experimental Method

[7] Tsukuba granite from Ibaraki Prefecture, Japan, was chosen for this study. It is a homogeneous rock with a fairly isotropic fabric, and the grain size ranges from 0.2 mm to 1.3 mm (coarser than Westerly granite), which is estimated from the optical microscopic observations at a magnification of 25 times. This granite has been used in previous studies on stick-slip and fracture experiments [e.g., *Ohnaka and Kuwahara*, 1990; *Ohnaka et al.*, 1997; *Odedra et al.*, 2001]. Approximate modal compositions are quartz 30%, feldspar 60%, biotite 5%, chlorite <5%, and muscovite <1% [*Odedra et al.*, 2001]. The average porosity, and density of Tsukuba granite are estimated to be 0.9%, and 2.65 g/cm^3, respectively. The permeability at room temperature, which was measured by the transient-method [*Yoshida*, 2001], is roughly 10^{-19} m^2 and decreases with an increase in effective confining pressure P_c^{eff} (= $P_c - P_p$) from 10 to 65 MPa (Table 1), which is around 5 times larger than that of Westerly granite [*Morrow et al.*, 1986]. This is because the grain size of Tsukuba-granite is coarser than that of Westerly granite. Cylindrical test specimens (length = 40 mm, diameter = 16 mm) were cored in the same direction, to an accuracy of within 0.02 mm. To saturate those samples with water before the experiments, they were submerged in distilled water after they had been kept in a container for air evacuation with a vacuum pump for 6–8 hours. Water saturation in the interstitial pores occurred after about 5 days.

[8] A triaxial testing apparatus recently constructed at E.R.I. was used for the present experiments. A detailed description of this apparatus is found in *Ohnaka et al.* [1997]. To establish the constitutive law for shear failure of rock, it is necessary to observe carefully the whole shear failure process with the apparatus in which the pre- and postfailure process is stabilized [e.g., *Hudson et al.*, 1972]. The apparatus is designed to stabilize the postfailure process by enhancing the stiffness of the loading system coupled to both high-response servo-hydraulics and a digital control system with 16-bit resolution. The intrinsic stiffness of the loading system (including sample assembly and pistons) is estimated to be 2000 ± 100 MPa/mm. Since the stiffness of the loading system is higher than that of the granite sample (1750 MPa/mm), the postfailure process was stabilized in the present experiments. The apparatus was designed to ensure high mechanical strength and toughness under the conditions of confining pressure (P_c) up to 500 MPa and temperature up to 500°C.

Table 1. The Permeability k of Tsukuba Granite Observed at a Variety of Effective Confining Pressures P_c^{eff} at Room Temperature

P_c^{eff} (*MPa*)	k (m^2)[a]
9.5	3×10^{-19}
19.1	1.8×10^{-19}
29.5	1.1×10^{-19}
48.0	0.51×10^{-19}
63.8	0.25×10^{-19}

[a] At room temperature.

[9] During each experiment, P_c was kept to within ±1.0 MPa and the temperature was kept to within ±0.5 °C. The axial load was measured with an external load cell placed between the actuator and the loading piston. The axial displacement of the loading piston was measured outside the pressure vessel with an LVDT, and its output signal was used as the feedback signal. The output signal measured for the axial load was corrected for the seal friction force. The seal friction force F at a load L was expressed by the relation F(ton) = $0.00808L$ (ton) + 0.387, which was not affected by the internal temperature [*Ohnaka et al.*, 1997]. The variation of seal friction during the application of axial load to sample was less than 10 MPa. The output signal of axial displacement was also corrected for integrated elastic deformation of the loading piston and of the inserted spacers.

[10] The cylindrical specimen was placed in a 2 mm-thick graphite sleeve (Figure 1). Given that graphite has higher porosity and much lower strength than granite, a graphite sleeve was used to minimize the possible gradient of pore pressure in the rock specimen, and it also served as a buffer to prevent the silver jacket (a 0.3 mm-thickness tube covering the sample assembly and piston spacers) from rupturing. The pore pressure (P_p), in the range of up to 400 MPa, was applied to the specimen through an axial hole in the lower loading piston. P_p was kept constant within ±0.5 MPa. Temperature was monitored by three thermocouples, located between the silver jacket and the furnace wall (Figure 1), and one of the thermocouples was used to control the temperature. The temperature difference over an axial direction of the specimen was found to be approximately 8% of the controlled temperature value.

[11] In order to prevent pores in a rock specimen from being isolated under high confining pressure, confining pressure P_c and pore pressure P_p were raised in step up to the desired test values. After these pressures had stabilized, temperature was raised at a constant rate of 3°C/min to the test run value, after which P_c, P_p and temperature were held constant by servo control for about 2 hours. In the present experiments, the strain rate was fixed at 10^{-5}/s, which corresponds to an axial displacement rate of 0.4 μm/s. All output signals for the axial load, the axial displacement, P_c, P_p and temperature were sampled at the frequency of 1 Hz with an analog-digital converter of 16-bit resolution.

[12] To investigate depth variation of the constitutive property, the experiments were conducted under simulated

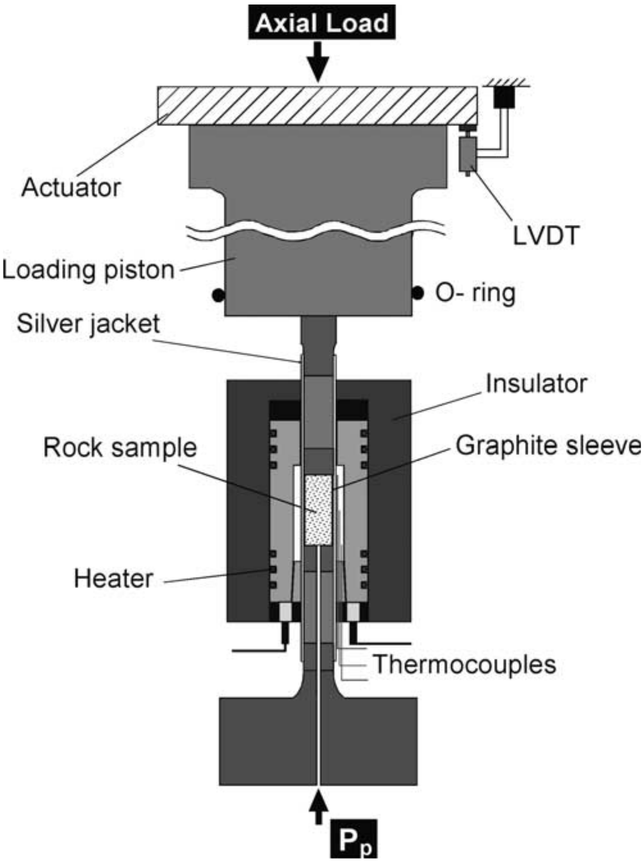

Figure 1. A sketch of sample and furnace configuration. The cylindrical specimen (40 mm long and 16 mm in diameter) is placed in a 2-mm-thick graphite sleeve. The sample is heated by an internal furnace of bobbin structure. The furnace is capped with a heat insulator housed in a stainless steel can. The pore pressure (P_p) is applied to the specimen through an axial hole of the lower loading piston.

crustal conditions. The temperature (geothermal) gradient was assumed to be 30°C/km, which is roughly close to the measured value in the borehole drilled down to 9.1 km achieved by the German Continental Deep Drilling Program (KTB) [*Clauser et al.*, 1997]. The lithostatic pressure gradient was assumed to be 30 MPa/km, which is slightly larger than the gradient derived from the density of granite. The temperature-pressure conditions assumed for the present experiments thus correspond roughly to a depth range down to 15 km in the seismogenic layer of the granitic crust.

[13] Since it is not clear how pore pressure is distributed in the seismogenic layer, two cases for the depth gradient of pore pressure were assumed. In one case, hydrostatic fluid-pressure gradient of 10 MPa/km was assumed (hydrostatic pore pressure regime). In fact, it was suggested that a pore fluid pressure in an in situ stress field obeys hydrostatic pressure gradient throughout the depth of the KTB borehole [e.g., *Huenges et al.*, 1997; *Zoback and Harjes*, 1997]. In the other case, suprahydrostatic fluid-pressure gradient of 24 MPa/km was assumed, which was 80% of the lithostatic pressure gradient (suprahydrostatic pore pressure regime). *Byerlee* [1990] and *Rice* [1992] independently proposed models in which pore pressure is elevated so as to sufficiently weaken the fault zone. There is some evidence that fluid pressure is greater than hydrostatic pressure during crustal deformation [*Moore et al.*, 1995; *Fisher and Zwart*, 1996].

3. Experimental Results

3.1. Constitutive Properties of Observed Data

[14] Since the fracture of intact rock occurs by shear mode under combined compressive stress conditions, it is appropriate to represent failure strength, in terms of the resolved shear strength along the macroscopic fracture plane, as a function of slip displacement (Figure 2). The corresponding slip displacement is the relative displacement between both walls of the fault zone thickness, which may include integrated amounts of slip associated with the deformation of asperity fractures, microcracking and local displacement between contacting gouge fragments. Note therefore that both shear strength and slip displacement used here for the constitutive formulation are defined in a macroscopic sense. The resolved shear strength τ, the slip displacement D and the resolved normal stress σ_n across the failure surface are calculated from the following equations

$$\tau = \frac{1}{2}(\sigma_1 - \sigma_3)\sin 2\theta \tag{1}$$

$$D = D_{app} - D_{el} = \frac{\Delta l}{\cos\theta} - \frac{\tau - a}{b} \tag{2}$$

$$\sigma_n = \frac{1}{2}(\sigma_1 - \sigma_3)(1 - \cos 2\theta) + \sigma_3. \tag{3}$$

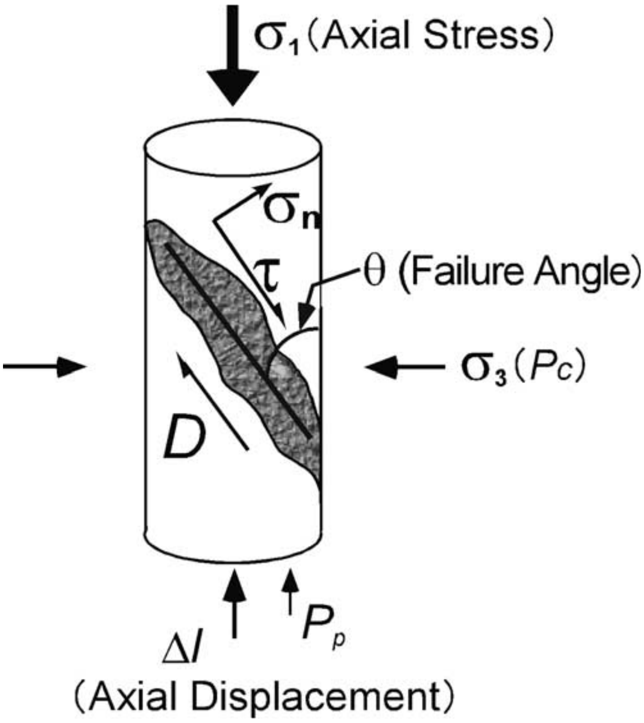

Figure 2. Illustration of a shear ruptured sample. The resolved shear and normal stresses, and slip displacement along the macroscopic fracture plane are represented by τ and σ_n, and D, respectively.

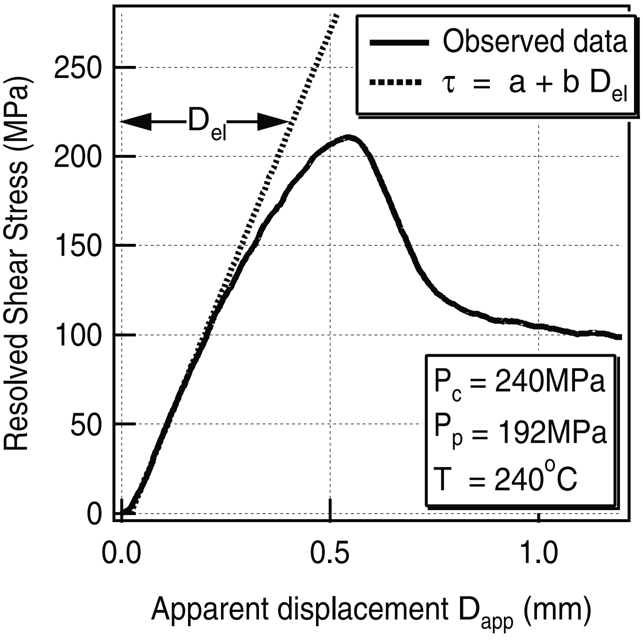

Figure 3. A plot of the resolved shear stress along the rupture surface against the apparent displacement under the conditions that simulate a crustal depth of 8 km, where the pore fluid pressure gradient has been assumed to be suprahydrostatic. The dashed linear line denotes the elastic deformation of the sample.

Here, θ is the failure angle between the macroscopic failure plane and the sample axis, σ_1 is the maximum principal stress, σ_3 is the minimum principal stress (which is equal to confining pressure in the present experiments) and Δl is the axial displacement of the sample. The first term ($D_{app} = \Delta l/\cos\theta$) on the right-hand side in equation (2) represents apparent slip along the failure plane, and the second term ($D_{el} = (\tau - a)/b$) indicates the correction for elastic deformation of the rock sample, when the linear line in Figure 3 is represented by $\tau = a + bD_{el}$, where a and b are constants.

[15] The failure angle of a tested sample was measured with a protractor after the silver jacket had been removed from the sample. In the present experiments, the macroscopic fault surfaces were formed, and they were able to be clearly observed even at high effective confining pressures, and therefore the failure angle θ was well measured. Figure 4 shows how θ varied under the test conditions selected for the present experiments. Black circles and white squares in the figure denote data on θ of the samples tested under the conditions of hydrostatic and suprahydrostatic pore pressures, respectively. It is found from Figure 4 that θ is almost constant within a range of 26° to 30° at simulated crustal depths shallower than 11 km, whereas θ tends to increase with increasing depth at depths greater than 11 km. The existing criterion for bulk plastic deformation predicts that the shear zone makes an angle of 45° against the maximum principal stress axis [e.g., *Jager and Cook*, 1976]. Thus the increase of θ at depths greater than 11 km is consistent with the existing criterion. Our sample observations indeed showed that some mineral grains experienced plastic deformation, which will be discussed in a later section.

[16] Figure 5 shows a typical example of the observed constitutive relation (thick curve) between τ and D under the condition simulating a crustal depth of 8 km, where the suprahydrostatic pore fluid pressure gradient of 24 MPa/km has been assumed. In Figure 5, τ_p is the peak shear strength, τ_r is the residual frictional strength, τ_{io} is the critical stress after which τ deviates from the linear-elastic line, D_c is the critical displacement required for τ to reach its peak value, D_c is the critical slip displacement required for τ to decrease to τ_r, $\Delta\tau_b$ is the breakdown stress drop defined as the difference between τ_p and τ_r, $|d\tau/dD|_{max}$ is the maximum slip-weakening rate during the breakdown process. Since the postfailure process is stabilized in the present experiments, note that the value of $|d\tau/dD|_{max}$ does not depend on the stiffness of the loading system. The apparent fracture energy G_c is defined as [*Palmer and Rice*, 1973; *Ohnaka and Yamashita*, 1989]

$$G_c = \int_{D_{co}}^{D_c} [\tau(D) - \tau_r]dD = \frac{\Gamma}{2}\Delta\tau_b D_c \quad [J/m^2], \qquad (4)$$

where D_{co} represents the relative displacement at which τ intersects with an extrapolation of the residual stress level τ_r, $\tau(D)$ is a function of representing the constitutive relation between τ and D, and Γ is a dimensionless

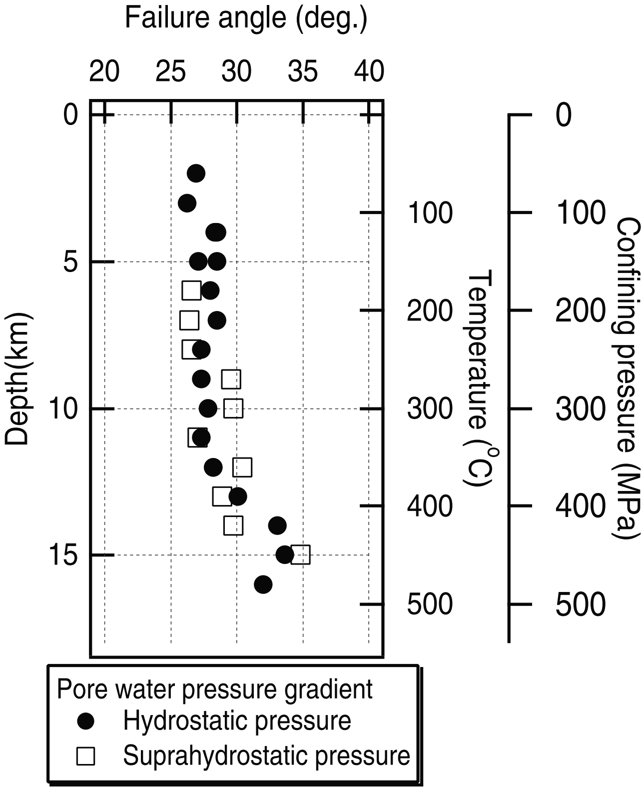

Figure 4. A plot of the failure angle θ observed at simulated crustal conditions against depth. Temperature and confining pressure corresponding to each crustal depth are also shown for reference. Black circles denote the failure angle of samples tested in the hydrostatic pore pressure regime, and white squares represent that of samples tested in the suprahydrostatic pore pressure regime.

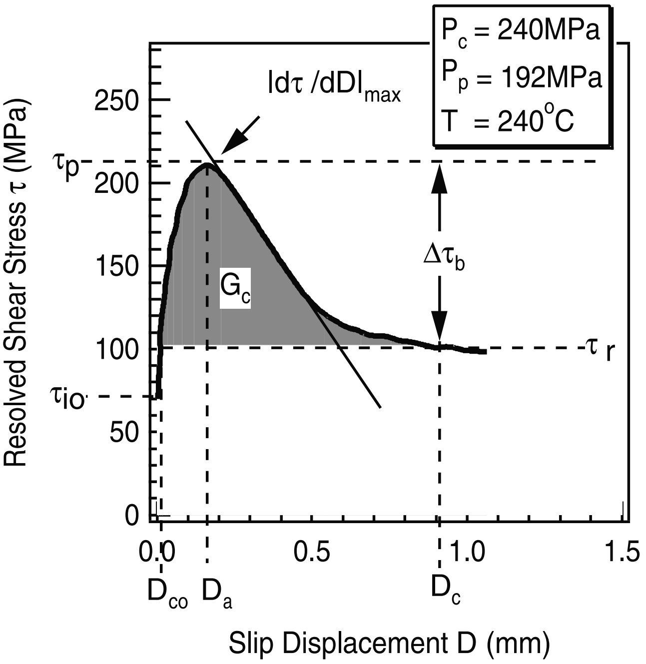

Figure 5. A typical example of the observed constitutive relation (thick curve) between τ and D under the same condition as shown in Figure 3. For symbols used, see text.

parameter dependent on a specific form of the function $\tau(D)$. Γ has been estimated to be around 1.0 for the shear fracture of intact granite [*Ohnaka et al.*, 1997]. Note that G_c defined by equation (4) equals the area of the shaded portion in Figure 5.

[17] As noted in an earlier paper [*Ohnaka et al.*, 1997], Figure 5 shows that τ initially increases with increasing D, and that after a peak value has been attained, τ degrades with ongoing slip during the breakdown process. The slip-strengthening phase preceding the slip-weakening phase has commonly been observed in high-resolution laboratory experiments on frictional slip failure along a preexisting fault [*Ohnaka and Yamashita*, 1989; *Ohnaka and Shen*, 1999]. In compressive loading of initially intact rock, pure elastic deformation is limited to the first 40–50% of τ_p (Figure 3). Above this level, nonelastic deformation develops progressively due to microprocesses such as crack growth, crack-crack interaction and coalescence in the brittle and brittle-plastic transition regimes. Lockner and his colleagues [e.g., *Lockner et al.*, 1991; *Reches and Lockner*, 1994] have demonstrated that the microcrack density becomes increasingly localized around a point where the peak shear strength is attained, from which the macroscopic shear failure surfaces eventually develop. We regard D_a as representing an integrated amount of slips caused by microcracking that necessarily occurs as a preparatory phase of imminent macroscopic failure. Without this preparatory phase, intact rock cannot fail macroscopically, and therefore it must be incorporated into the constitutive relation.

[18] One may argue that the shear stress before failure ($D < D_c$) may not be related to the fault orientation after failure ($D > D_c$), and that our approach for the stress analysis mentioned above is problematic. However, it has recently been demonstrated by using laboratory data on both shear failure of intact rock and frictional slip failure that a direct proportional relationship exists between D_a and D_c [*Ohnaka*, 2000b; *Ohnaka*, 2003]. This indicates that the preceding process of displacement-hardening can substantially prescribe the displacement-weakening process, suggesting that D_c and D_c may be described in terms of the common, underlying physics. It is therefore well grounded that the displacement-hardening process before failure cannot be physically irrelevant to the displacement-weakening process after failure. In addition, the present approach makes it possible to provide a unified understanding of scale-dependent physical quantities inherent in the rupture of a wide scale [see *Ohnaka*, 2000a and 2000b; *Ohnaka*, 2003]. Hence, the present approach is not only physically grounded but also significant and useful for unifying the shear failure that is inherently scale-dependent, in the consistent framework of fracture mechanics.

[19] In Figure 6, the constitutive relations observed in the hydrostatic pore pressure regime are compared with those observed in the suprahydrostatic regime. It is obvious from this figure that the shear strength tested at suprahydrostatic pore pressures is much weaker than that tested at hydrostatic pressures. This is because the effective confining pressure is lower at suprahydrostatic pore pressures. We find from Figure 6 that $|d\tau/dD|_{max}$ in both hydrostatic (56 MPa/mm) and suprahydrostatic (93 MPa/mm) regimes at a simulated

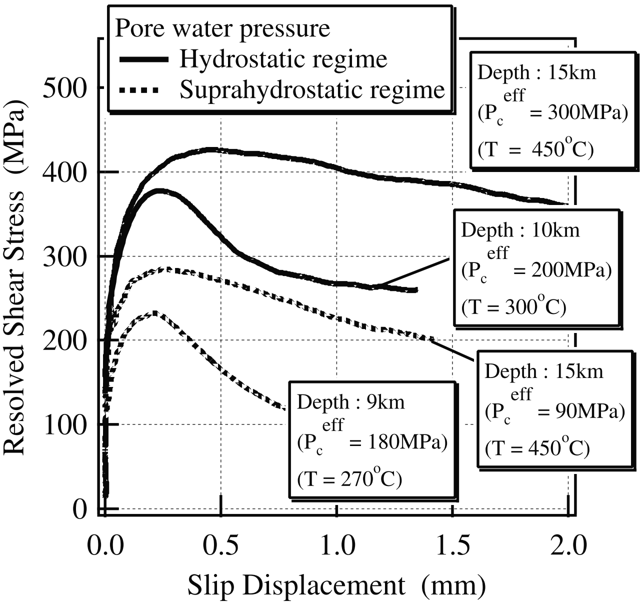

Figure 6. Typical examples of constitutive relations observed under the simulated crustal conditions. Solid curves represent data observed in the following hydrostatic regime: (1) P_c = 300 MPa, P_p = 100 MPa, and T = 300°C, corresponding to a crustal depth of 10 km; and (2) P_c = 450 MPa, P_p = 150 MPa, and T = 450°C, corresponding to a crustal depth of 15 km. Dotted curves denote data observed in the following suprahydrostatic regime: (1) P_c = 270 MPa, P_p = 216 MPa, and T = 270°C, corresponding to a crustal depth of 9 km; and (2) P_c = 450 MPa, P_p = 360 MPa, and T = 450°C, corresponding to a crustal depth of 15 km.

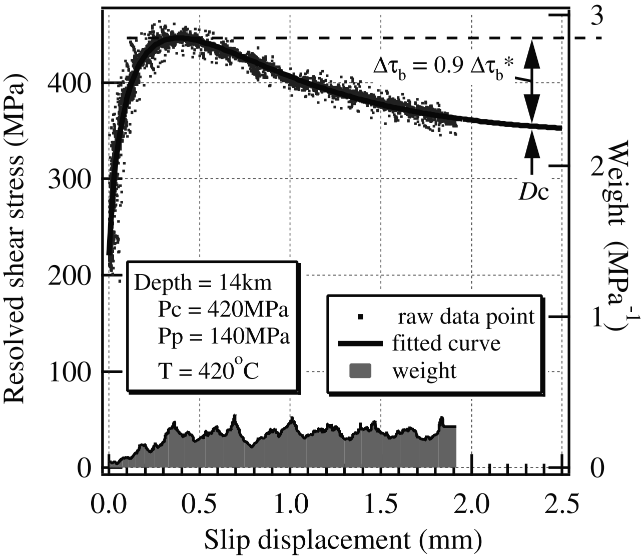

Figure 7. An example of the results of the iterative, least squares method applied to a set of observed data points, which were obtained at the following test conditions: P_c = 420 MPa, P_p = 140 MPa (hydrostatic pore pressure), and T = 420°C, corresponding to a crustal depth of 14 km. A thick line represents the best-fitted curve, and the observed set of data points is well represented by the fitted curve. The calculated components of weighting vector are shown at the bottom of the figure.

crustal depth of 15 km is much less than $|d\tau/dD|_{\max}$ in those regimes (282 MPa/mm at hydrostatic, 262 MPa/mm at suprahydrostatic regime) at depths shallower than 10 km. This means that the breakdown process is more stable at a depth of 15 km than at a depth of 9 or 10 km.

3.2. Evaluation of Constitutive Law Parameters

[20] In order to quantify depth variations in the constitutive parameters D_c, $\Delta\tau_b$ and τ_p, we evaluate these parameters from observed constitutive relations. In some cases in which temperature is greater than 360°C, however, it was difficult to determine the values for these parameters directly from the observed constitutive relations, because the silver jacket had broken before the shear strength had decreased to a residual friction stress level τ_r. In these cases, we firstly obtained the best-fitted curve to the observed data and then estimated the constitutive parameters D_c and $\Delta\tau_b$ from the fitted curve (Figure 7), as described below.

[21] An observed constitutive relation between τ and D can be represented by the following empirical slip-dependent constitutive equation [*Ohnaka and Yamashita*, 1989; *Ohnaka*, 1996]

$$\begin{aligned}\tau(D) &= \tau_p - \Delta\tau_b^* + \Delta\tau_b^*(1 + A\log[1 + B(D/D_a - 1)]) \\ &\quad \cdot \exp[-AB(D/D_a - 1)],\end{aligned} \tag{5}$$

where both A and B are unknown model parameters independent of D, and $\Delta\tau_b^*$ is the breakdown stress drop

Table 2. Constitutive Parameters Evaluated Under the Two Simulated Crustal Conditions: Hydrostatic and Suprahydrostatic Pore Pressure Regimes[a]

Depth, km	P_c, MPa	Temp, °C	P_p, MPa	Θ, deg	τ_p, MPa	τ_ι, MPa	D_a, mm	D_c, mm	$\Delta\tau_b$, MPa	$\lvert d\tau/dD\rvert_{\max}$, MPa/mm	G_c, kJ/m^2	A	B
						Hydrostatic Pore Water Pressure							
2	60	60	20	26.9	215.0	65.0	0.181	0.80	128.0	233.1	52.9		
3	90	90	30	26.2	232.0	102.0	0.176	1.00	140.0	292.3	60.3		
4	120	120	40	28.3	268.2	126.0	0.222	1.23	121.2	197.5	68.9		
4	120	120	40	28.5	259.7	129.0	0.170	1.32	132.6	197.4	77.4		
5	150	150	50	28.5	313.7	118.5	0.200	0.82	123.7	343.2	46.4		
5	150	150	50	27.1	290.4	124.0	0.215	0.85	114.0	341.1	46.4		
6	180	180	60	28.0	320.0	131.0	0.236	0.83	106.4	333.2	39.4		
7	210	210	70	28.5	350.0	164.5	0.223	1.05	130.0	240.2	63.5		
8	240	240	80	27.3	367.4	171.0	0.210	0.95	128.4	344.6	50.0		
9	270	270	90	27.3	367.1	182.5	0.192	0.85	112.4	354.2	37.1		
10	300	300	100	27.8	377.9	182.0	0.234	1.02	111.0	282.3	48.7		
11	330	330	110	27.3	398.7	183.0	0.240	1.08	104.7	256.0	46.5		
12	360	360	120	28.2	398.9	220.0	0.280	1.60	87.4	110.7	61.7	0.795	0.835
13	390	390	130	30.1	423.4	210.0	0.345	1.84	102.5	113.7	83.5	0.942	0.778
14	420	420	140	33.1	445.9	220.0	0.385	2.36	92.4	79.1	95.1	0.655	0.921
15	450	450	150	33.6	426.5	200.0	0.463	3.00	83.5	55.7	109.6	0.581	0.958
16	480	480	160	32.0	397.0	168.0	0.428	3.53	61.3	34.8	92.0	0.42	0.998
						Suprahydrostatic							
6	180	180	144	26.6	187.9	76.0	0.167	0.80	106.6	313.4	39.6		
7	210	210	168	26.4	195.5	85.0	0.181	0.83	102.2	289.4	41.8		
8	240	240	192	26.6	210.7	70.0	0.162	0.73	103.0	307.8	34.4		
9	270	270	216	29.6	232.4	108.0	0.209	0.97	125.6	262.0	57.7		
10	300	300	240	29.7	258.5	140.0	0.165	0.99	105.8	212.0	48.5		
11	330	330	264	27.0	241.6	91.0	0.213	0.95	115.6	317.8	52.1		
12	360	360	288	30.4	240.8	135.0	0.180	1.33	108.7	160.0	64.9	0.61	0.778
13	390	390	312	28.9	246.0	130.0	0.210	1.77	111.0	122.8	86.2	0.454	0.878
14	420	420	336	29.7	252.8	116.0	0.265	2.15	133.4	122.0	126.6	0.494	0.852
15	450	450	360	34.8	284.0	155.0	0.260	2.29	109.2	92.9	108.6	0.413	0.922

[a] Both A and B are model parameters determined from the fitting-procedure. For details on the method, see text.

at infinite D. The parameters A and B are constrained by the following relation

$$\Delta\tau_b^* = \frac{\tau_p - \tau_{io}}{1 - (1 + A\ \log[1 - B])\exp[AB]}. \qquad (6)$$

[22] The values of the constitutive parameters τ_p, τ_{io}, and D_a are known, because they are evaluated directly from the constitutive curve smoothed from observed raw data. Since equation (5) is nonlinear with respect to the unknown model parameters A and B, an iterative, least squares method [*Press et al.*, 1992] was used to solve this nonlinear inverse problem. The weighting vector components were defined as the inverse of the standard deviation of noise for the raw data, and were calculated by moving each window consisting of 100 data points.

[23] Figure 7 shows an example of the results of the iterative, least squares method applied to observed data points, which were obtained at the following test conditions: P_c = 420 MPa, P_p = 140 MPa (hydrostatic pore pressure), and T = 420°C (simulated crustal depth of 14 km). A thick solid line in the figure represents the best-fitted curve, and values for τ_p, τ_{io} and D_a used in the inversion were 445.9 MPa, 220 MPa and 0.385 mm, respectively. We find that the fitted curve well represents the observed set of data points. The weighting vector components calculated are shown at the bottom of Figure 7, as a function of slip displacement D. The effective breakdown stress drop $\Delta\tau_b$ was defined here as $\Delta\tau_b = 0.9\Delta\tau_b^*$, and D_c was defined as the corresponding displacement. The uncertainties of the estimates of $\Delta\tau_b$ and D_c come from the uncertainties of the parameters A, B and D_a (±3–8%), and they were ±(3–10)% for $\Delta\tau_b$, and ±(3–8)% for D_c. The constitutive parameters (D_c, $\Delta\tau_b$, $|d\tau/dD|_{\max}$ and G_c) evaluated are listed in Table 2.

3.3. The Depth Variation of Constitutive Law Parameters

[24] We here discuss how the constitutive law parameters determined from constitutive relations observed in the laboratory experiments vary with simulated crustal depth.

3.3.1. Peak Shear Strength τ_p

[25] The peak shear strength τ_p evaluated in this study is plotted against a simulated crustal depth in Figure 8. As expected from the difference in the effective confining pressure, τ_p at suprahydrostatic pore pressures (white squares) has much lower values than it does at hydrostatic pore pressures (black circles). It is seen from this figure that τ_p increases linearly with increasing depth in a layer shallower than 9 or 10 km. At depths greater than 9 or 10 km, however, τ_p is lower than that extrapolated from the above linear relations (solid lines). This is because wet granite is more weakened by the effect of temperature above about 300°C at confining pressures corresponding to depths greater than 9 or 10 km. This suggests that wet granite under these conditions is in the brittle-plastic transition regime, which is indeed corroborated from microscopic observation of the operative mechanism of deformed samples (see section 3.4).

[26] Linear lines shown in Figure 8 have been determined by the least squares fit to individual data sets obtained at the crustal conditions corresponding to depths shallower than 9 or 10 km. The reason for this is as follows. At depths shallower than 9 or 10 km, which is in the brittle regime, the peak shear strength τ_p is expected to be a linear function of depth, because τ_p linearly depends on the effective normal stress, but because it is insensitive to temperature in the brittle regime. However, at depths deeper than 9 or 10 km, which is in the brittle-plastic transition regime, τ_p can no longer be a linear function of depth. This is because τ_p depends on both effective normal stress and temperature, and because τ_p is suppressed by the effect of an increasing temperature with an increasing depth in the transition regime. In view of this, therefore, it is not appropriate to apply a linear fit to the entire data set including those obtained at the crustal conditions deeper than 9 or 10 km.

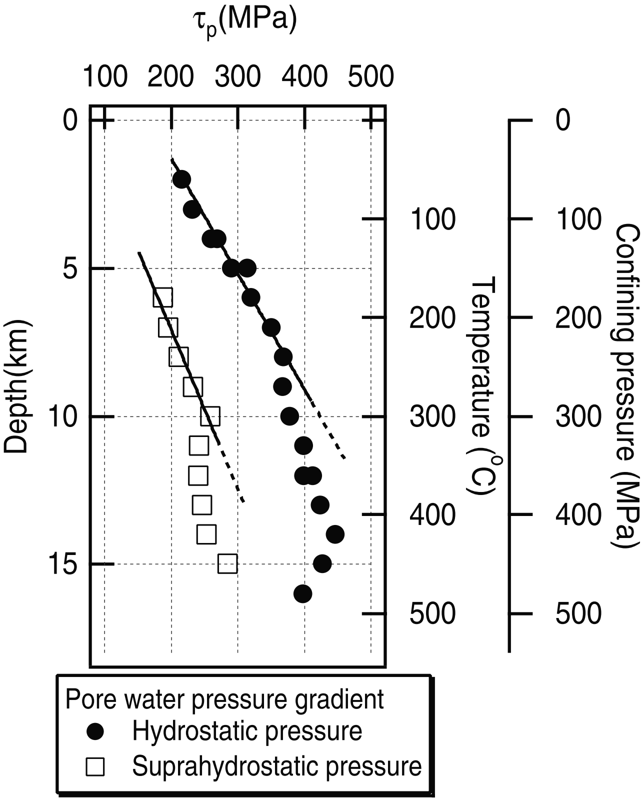

Figure 8. The variation of τ_p against simulated crustal depth. Black circles denote τ_p obtained at hydrostatic pore pressures, and white squares represent τ_p obtained at suprahydrostatic pore pressures. The linear relation between τ_p and depth can be expressed by, $\tau_p = 165 + 25 \times \mathit{depth}$ for the hydrostatic regime, and $\tau_p = 68 + 18.5 \times \mathit{depth}$ for the suprahydrostatic regime.

[27] Note that even above 300°C, there is a significant difference in τ_p between hydrostatic and suprahydrostatic pore pressure regimes, and that the pressure effect on τ_p still exists above 300°C. This indicates that τ_p depends on both temperature and effective normal stress above 300°C. It will be shown in section 4.1 that the effective stress law holds for the present data set.

3.3.2. Critical Slip Displacement D_c

[28] Figure 9 shows a plot of D_c obtained in the present experiments against a simulated crustal depth. In this plot, D_c has been normalized to the value of D_{co} = 0.87 mm, which is the average value for D_c observed at simulated depths ranging from 6 km to 9 km. The reason for this

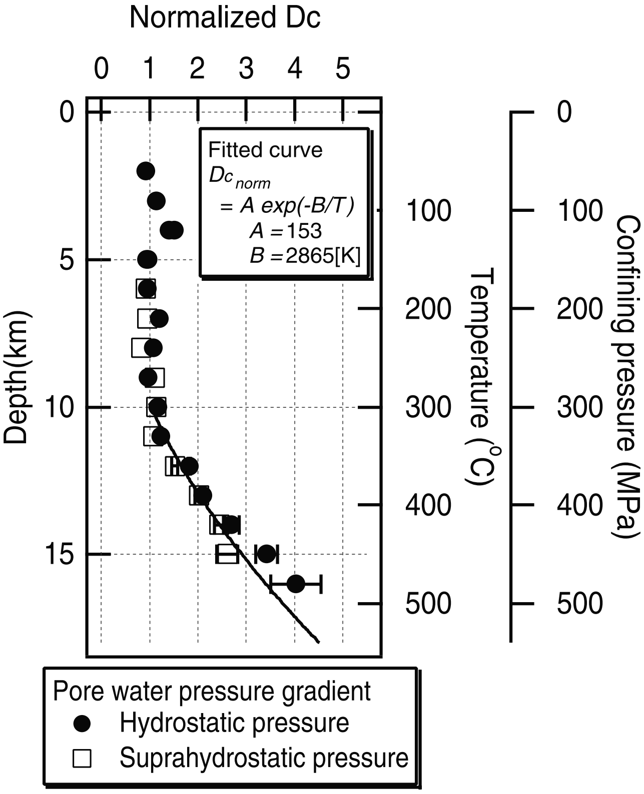

Figure 9. A plot of D_c normalized to D_{co} = 0.87 mm against simulated crustal depth. Black circles denote D_c obtained at hydrostatic pore pressures, and white squares represent D_c obtained at suprahydrostatic pore pressures. The error bar of data points shows the uncertainty of D_c determined by the fitting. The solid curve is the fitted curve to the data points for Dc above 300°C using equation (9).

normalization is that D_c is inherently scale-dependent, and that the amount of D_c for small-scale rupture in the laboratory is much smaller than that for large-scale earthquake rupture in the field [see *Ohnaka and Shen*, 1999; *Ohnaka*, 2000a, 2000b; *Ohnaka*, 2003]. It is therefore not appropriate but misleading to plot absolute values of the scale-dependent D_c obtained in the laboratory against a simulated crustal depth, without considering its scale-dependence. Scaling of scale-dependent constitutive properties is beyond the scope of the paper.

[29] It is found from Figure 9 that D_c can be regarded as virtually constant under the conditions of depths shallower than 10 km, and that D_c increases with increasing depth at depths greater than 10 km. Note that D_c at a depth of 15 km, is about three times larger than D_c at depths shallower than 10 km. These observations indicate that D_c above 300°C becomes sensitive to temperature and less sensitive to effective confining pressure. This implies that an increase in D_c above 300°C is primarily due to a thermally activated process. The effect of temperature on D_c above 300°C can be expressed by the following equation [*Ohnaka*, 1992]

$$\overline{D_c} = A\ \exp\left(-\frac{B}{T}\right) \qquad \text{for T} > 573\text{K} \tag{7}$$

where $\overline{D}_c$ denotes the normalized D_c, A and B are constants and T is the absolute temperature. The least squares fit to the data on D_c above 300°C gives $A = 153$ and $B = 2865$ [K]. It is corroborated from the present data set that equation (7) well represents the dependence of D_c on temperature above 300°C.

[30] *Ohnaka* [1992] proposed a model of depth profile for D_c for a given geotherm, based mainly on dry experimental results by *Wong* [1982]. Although Ohnaka's model is similar to the present results, the depth profile of D_c in seismogenic, wet environments was not well constrained, because of the limited number of available data on D_c. It is in the present study that a depth profile for D_c in wet environments has been evaluated successfully from laboratory data. It is estimated from Wong's results (using Westerly granite) that the amount of (D_c − D_a) is around 0.3 mm below 300°C. The amount of 0.3 mm is roughly half the amount of (D_c − D_a) from the present data set. This difference may be ascribed to the difference of grain size, because the amounts of D_a and D_c depend on geometric irregularity of the rupturing surfaces [*Ohnaka*, 2000b; *Ohnaka*, 2003], and because the geometric irregularity can be prescribed by structural heterogeneity of rock fabric including grain size.

3.3.3. Breakdown Stress Drop $\Delta\tau_b$

[31] In Figure 10, $\Delta\tau_b$ is plotted against a simulated crustal depth. From this figure, it is found that $\Delta\tau_b$ in the hydrostatic and suprahydrostatic pore pressure regimes is roughly 100 MPa in a simulated crustal depth range down to 15 km, though $\Delta\tau_b$ in the hydrostatic regime tends to decrease gradually with increasing depth. It has been shown

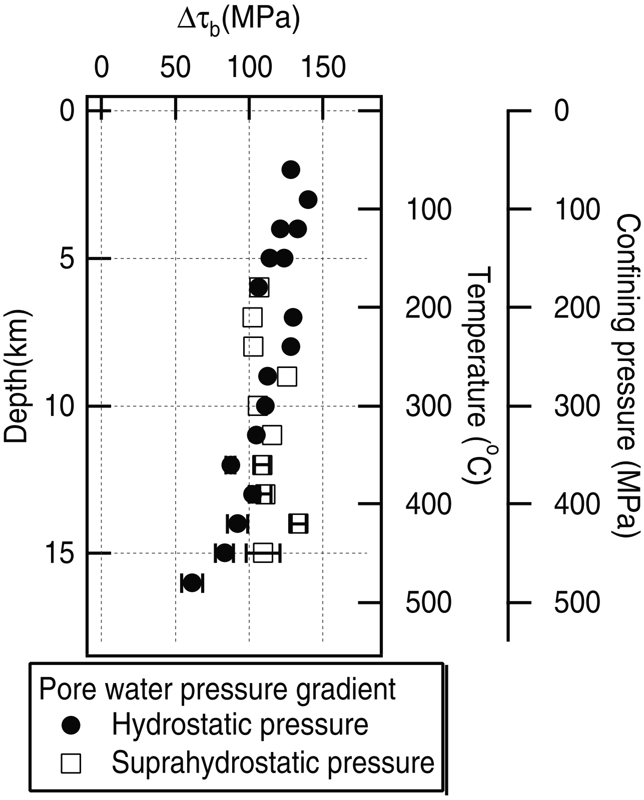

Figure 10. A plot of $\Delta\tau_b$ against simulated crustal depth. Black circles denote $\Delta\tau_b$ obtained at hydrostatic pore pressures, and white squares represent $\Delta\tau_b$ obtained at suprahydrostatic pore pressures.

in previous experiments on granite at room temperature and at dry conditions [*Wong*, 1982, 1986] that $\Delta\tau_b$ can be regarded as virtually constant over a range of confining pressure from 100 to 300 MPa. It may thus be concluded that $\Delta\tau_b$ for intact granite is virtually constant under the conditions simulating the brittle regime below 300°C.

3.3.4. Maximum Slip-Weakening Rate $|d\tau/dD|_{max}$

[32] Whether a portion of a fault zone breaks down stably or unstably depends on the relationship between crustal stiffness k at that portion and the maximum slip-weakening rate $|d\tau/dD|_{max}$. If k is smaller than $|d\tau/dD|_{max}$, the breakdown near the rupture front proceeds unstably and dynamically, and elastic waves are radiated. If, however, k is larger than $|d\tau/dD|_{max}$, the breakdown proceeds stably and quasi-statically, and no elastic waves are radiated. Hence, $|d\tau/dD|_{max}$ is an crucial parameter for determining the instability or stability of the breakdown process.

[33] Figure 11 shows a plot of $|d\tau/dD|_{max}$ against simulated crustal depth. In this figure, $|d\tau/dD|_{max}$ has been normalized to 305 MPa/mm, which is a representative value of $|d\tau/dD|_{max}$ in the brittle regime below 300 °C. In this plot, $|d\tau/dD|_{max}$ has been normalized because of its scale-dependence. We find from Figure 11 that $|d\tau/dD|_{max}$ does not depend on depth at depths shallower than 10 km, in both hydrostatic and suprahydrostatic pore pressure regimes. This is because $|d\tau/dD|_{max}$ is insensitive to both temperature and effective confining pressure below 300°C. At simulated crustal depths greater than 10 km, however, $|d\tau/dD|_{max}$ decreases sharply with increasing depth, and the amount of $|d\tau/dD|_{max}$ at a depth of 15 km becomes about one-fifth of $|d\tau/dD|_{max}$ at depths shallower than 10 km. This is because a decrease in $|d\tau/dD|_{max}$ is caused by an increase in temperature. Figure 11 leads to the conclusion that the mechanical stability is enhanced at these greater depths.

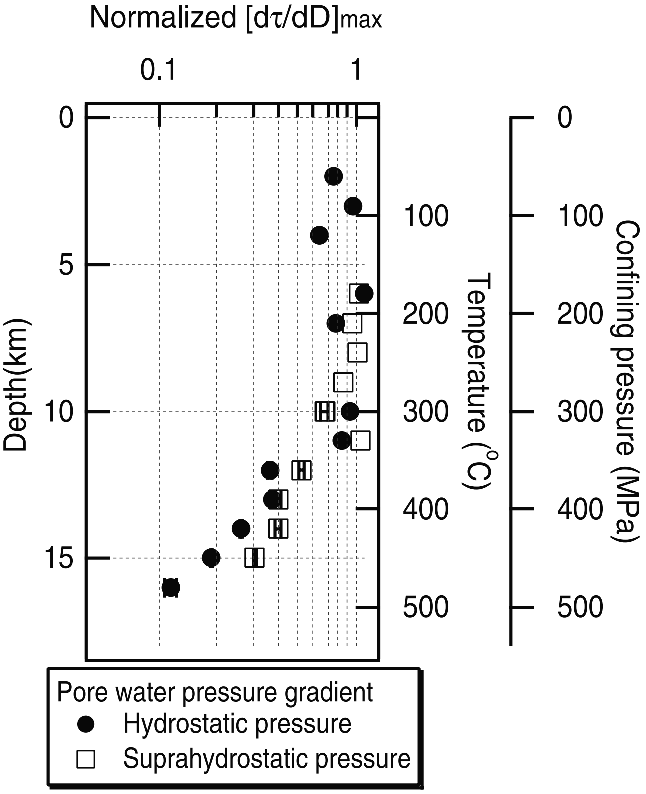

Figure 11. A plot of $|d\tau/dD|_{max}$ normalized to 305 MPa/mm against simulated crustal depth. Black circles denote $|d\tau/dD|_{max}$ obtained at hydrostatic pore pressures, and white squares represent $|d\tau/dD|_{max}$ obtained at suprahydrostatic pore pressures.

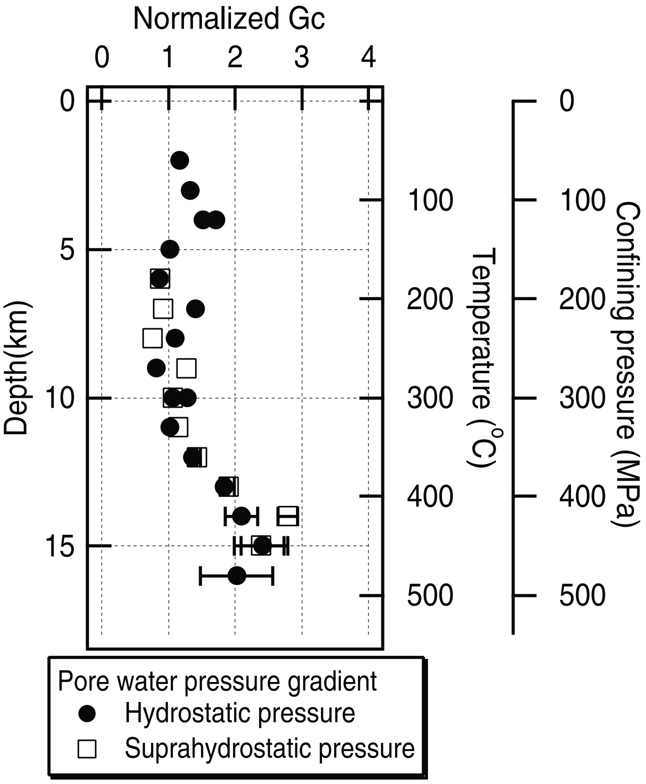

Figure 12. A plot of G_c normalized to 4.5×10^4 J/m^2 against simulated crustal depth. Black circles denote G_c obtained at hydrostatic pore pressures, and white squares represent G_c obtained at suprahydrostatic pore pressures.

3.3.5. Apparent Fracture Energy G_c

[34] The apparent fracture energy G_c represents the resistance to rupture growth, and hence it influences whether the rupture front grows or arrests. Figure 12 shows a plot of G_c against simulated crustal depth. Since G_c is calculated from equation (4), the amount of G_c is necessarily scale-dependent, because D_c is scale-dependent [*Ohnaka*, 2000a, 2000b; *Ohnaka*, 2003]. For this reason, G_c has also been normalized (to the value of $G_c = 4.5 \times 10^4$ J/m^2), and the normalized G_c is plotted in Figure 12.

[35] It is found from Figure 12 that G_c is roughly constant under the conditions of simulated crustal depths shallower than 10 km, and that G_c tends to increase at greater depths, becoming nearly 2.5 times larger at a depth of 15 km. The increase in G_c at greater depths results from the increase in D_c, because $\Delta\tau_b$ does not vary greatly. It can thus be concluded that the increase in G_c at depths greater than 10 km is primarily due to the effect of temperature, because an increase in D_c at greater depths is caused by temperature.

3.4. Sample Observations

[36] Observations of naturally and experimentally formed faults have revealed that the faults are not simple discrete planar surfaces. While discrete faults are formed, a more

diffuse deformation occurs within a volume of material surrounding these fault surfaces (damage zone). Studies of damage zones around fault surfaces have classified the zones into two types: cataclasite and process zones [e.g., *Scholz et. al.*, 1993; *Reches and Lockner*, 1994; *Moore and Lockner*, 1995]. In the cataclasite zone, cataclastic gouges and Reidel shears develop. In the process zone, open cracks subparallel to the maximum principal stress are dominant.

[37] Information about the operative mechanism during the shear failure of intact Tsukuba granite and about the internal structure of the damage zone can be obtained by microscopic examination of thin sections from samples tested. For samples deformed at the condition simulating a crustal depth of 6 km in the suprahydrostatic pore pressure regime, the width of a cataclasite zone was in a range from 0.14 mm to 0.3 mm along the fault length. It was clearly observed that the cataclasite zone was mainly filled with cataclastic gouges. Neither quartz nor feldspar exhibited plastic deformation. Some biotite near the damage zone, whose basal plane had been perpendicular to the cataclasite zone, was bent and crosscut brittly due to the relative displacement of the damage zone (Figure 13a). Although the plasticity of biotite was also observed in the cataclasite zone of samples tested at temperatures lower than 300°C, the degree of plasticity was not so high at those lower temperatures.

[38] For samples tested at a simulated crustal depth of 14 km in the hydrostatic pore pressure regime, the number of cracks subparallel to the cataclasite zone was found to increase around its boundary in the damage zone. The width of the cataclasite zone was in a range from 0.2 mm to 0.42 mm. It was remarkable that biotite within the cataclasite zone was elongated subparallel to the slip displacement (Figure 13b). This indicates that biotite was completely deformed plastically at those conditions. Quartz near the edge of the cataclasite zone showed a little undulatory extinction at a simulated crustal depth of 15 km in the hydrostatic pore pressure regime, though the preferred orientation of the grain was not observed (Figure 13c). Feldspar remained brittle in the entire range of the present test conditions, with no undulatory extinction. These microscopic observations suggest that full plastic deformation of biotite and a little amount of plastic deformation of quartz occurred above 300°C in the presence of pore water.

[39] In order to investigate the damage zone property, we estimated the microcrack density in the damage zone as a function of the length in the direction perpendicular to the fault. The damage zone is defined here as the localized zone

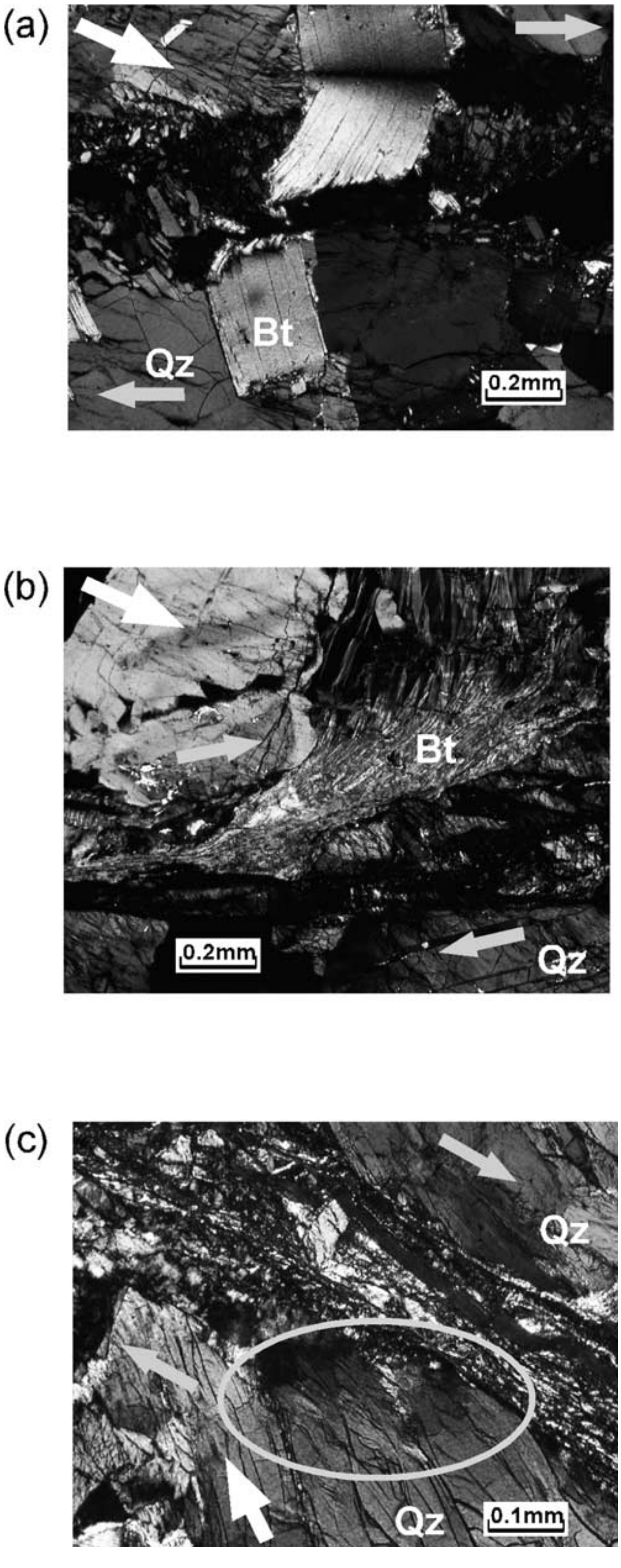

Figure 13. (opposite) Photo-micrographs around the damage zone for tested samples. Yellow arrow and white arrow in each figure denote the slip direction and the maximum stress orientation, respectively. Bt and Qz denote grains of biotite and quartz, respectively. (a) Biotite near the damage zone, of which basal plane had been perpendicular to the cataclasite zone, was bent and crosscut brittly due to the relative displacement of damage zone. This sample was deformed at the condition corresponding to a simulated crustal depth of 6 km: (P_c, P_p, T) = (180 MPa, 144 MPa, 180°C). (b) Biotite within the cataclasite zone was elongated subparallel to the slip displacement, which indicates that biotite was deformed fully plastically at a depth of 14 km: (P_c, P_p, T) = (420 MPa, 140 MPa, 420°C). (c) Quartz near the edge of cataclasite zone (area enclosed with white line) showed undulatory extinction at a depth of 15 km: (P_c, P_p, T) = (450 MPa, 150 MPa, 450°C). See color version of this figure at back of this issue.

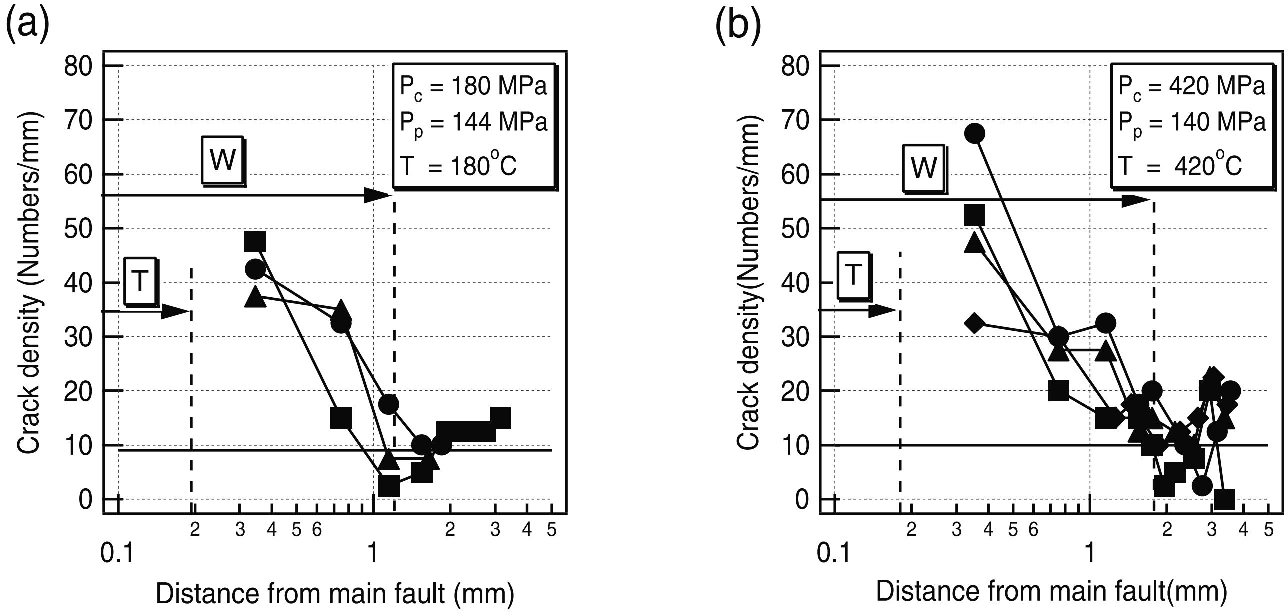

Figure 14. The relation between microcrack densities and the distance from the center of the cataclasite zone in deformed samples under the conditions corresponding to (a) a crustal depth of 6 km in the suprahydrostatic regime (P_c, P_p, T) = (180 MPa, 144 MPa, 180°C), and (b) a crustal depth of 14 km in the hydrostatic regime (P_c, P_p, T) = (420 MPa, 140 MPa, 420°C). *W* denotes the width of the damage zone and *T* represents the average width of the cataclasite zone.

along the fault, where the microcrack density is significantly high compared with its background level (see Figure 14). The microcrack density is defined as the number of microcracks per unit length. The number of microcracks was counted, at a magnification of 100 times, by moving a 0.4 mm length window along a line perpendicular to the fault from the edge of the cataclasite zone. The measurements were conducted along several lines perpendicular to the fault, and the average values were calculated to represent the crack density of the damage zone for each fault.

[40] Figure 14 shows the relation between the microcrack density obtained and the distance from the center of the cataclasite zone for samples tested under the conditions simulating a crustal depth of 6 km in the suprahydrostatic pore pressure regime (Figure 14a), and 14 km in the hydrostatic pre pressure regime (Figure 14b). The microcrack density at positions distant from the fault was also measured to know its background level, and the background density level is shown by a horizontal line in the figure. From Figure 14, the width of the damage zone can be defined as denoted by *W*. *T* in the figure represents the average width of the cataclasite zone. It is found from this figure that the microcrack density decreases logarithmically to its background level with increasing distance. This feature was commonly observed for damage zones of other tested samples. The present result agrees with previous observations of naturally deformed damage zones of faults in the field. *Vermilye and Scholz* [1998] provided detailed observations of naturally deformed damage zones of faults by measuring microcrack densities, and they have found that microcrack densities for several faults decrease logarithmically as a function of distance from the fault plane.

[41] Figure 14 shows that the damage zone width (*W*) for Tsukuba granite is roughly 1 mm. One may also notice from Figure 14 that the damage zone width (*W*) at a simulated crustal depth of 14 km is slightly larger than that at a depth of 6 km. This is consistent with the fact that the damage zone width tends to be larger in the brittle-plastic transition regime. In the present experiments, the total amount of slip displacement is almost the same within a factor of two during the deformation of individual samples, and hence the effect of slip amounts on the damage zone width is negligible.

4. Discussion

4.1. Effective Stress Law

[42] It has been found from the present experiments that pore water pressure in a rock sample significantly affects the shape of the constitutive curve (Figure 6). It is well known, however, that dilatant microcrack growth during the breakdown process can cause dilatancy hardening if the diffusivity of pore water is slower than the microcrack growth rate [*Paterson*, 1978; *Lockner and Byerlee*, 1994]. *Brace and Martin* [1968] reported that the effective stress law did not hold for Westerly granite samples tested at a strain rate of 10^{-5}/s, and that the critical strain rate for obeying the effective stress law was less than 10^{-7}/s in their experimental configuration at room temperature. One may therefore argue that our data set may be contaminated by the dilatancy-hardening effect. We wish to demonstrate here that the effective stress law indeed holds for our data set tested at a strain rate of 10^{-5}/s in the present experimental configuration, and that the critical strain rate depends on the experimental configuration.

[43] The present experimental configuration is similar to that of *Brace and Martin* [1968], except that the Tsukuba granite sample was inserted into a porous graphite sleeve (see Figure 1). In order to demonstrate how effectively the

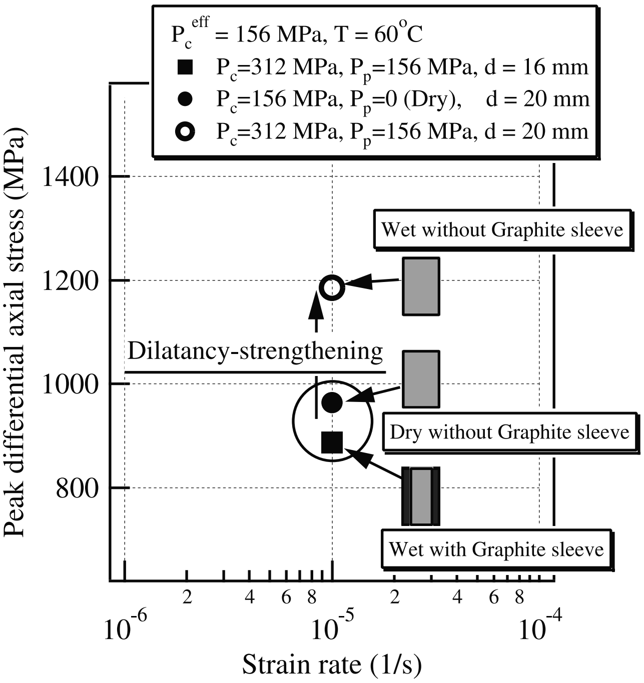

Figure 15. Observed peak differential axial stresses σ_d for different sample configurations and test conditions. The nominal effective confining pressure was set to be 156 MPa for all the experiments shown in the figure.

graphite sleeve helps for water fluid to permeate pore spaces in the sample, we conducted a series of experiments under the following conditions. We set the nominal effective confining pressure P_c^{eff} to be 156 MPa for this series of experiments (Figure 15). In one experiment where a test sample was deformed at a strain rate of 10^{-5}/s without a graphite sleeve (sample diameter 20 mm) under a dry condition (P_c, P_p, T) = (156 MPa, 0 MPa, 60°C), the peak differential axial stress σ_d of 964 MPa was obtained. In another experiment where a test sample was deformed at the same strain rate without a graphite sleeve (sample diameter 20 mm) under a wet condition (P_c, P_p, T) = (312 MPa, 156 MPa, 60°C), σ_d of 1148 MPa was obtained. It is thus obvious from these two sets of data that the effective stress law does not hold, because there is a significant difference (20%) in σ_d between the two experiments in spite of the same nominal effective pressure. This is consistent with the conclusion by *Brace and Martin* [1968].

[44] However, in the experiment where a test sample (its diameter 16 mm) inserted into a graphite sleeve was deformed at the strain rate of 10^{-5}/s under a wet condition (P_c, P_p, T) = (312 MPa, 156 MPa, 60°C), σ_d of 890 MPa was obtained. The value of 890 MPa for σ_d is 7.7% lower than that observed under the dry condition; however, this difference is not necessarily significant, given the experimental errors inevitably involved. Even if the difference can be regarded as significant, it will be attributed to chemical effect of water (enhancement of subcritical crack growth in wet environments). It can thus be concluded that the effective stress law holds for Tsukuba granite deformed at a strain rate of 10^{-5}/s, when the sample is inserted into a porous graphite sleeve.

[45] We check here if the conclusion that the effective stress law holds in our experimental configuration can be validated theoretically. Consider a case where interstitial pore water pressure drops at the inner portion of a rock sample due to the dilatancy-hardening effect. In this case, the characteristic time t_c for the pore pressure to return to its original value is given from the diffusion theory as [*Crank*, 1975]

$$t_c = 2L_s^2/D, \tag{8}$$

where L_s is the length of a region in which interstitial pore pressure drops, and D is the diffusion coefficient. If the compressibility of fluid is much larger than that of rock, the diffusion coefficient can approximately be represented as $D = k/(\mu\beta\eta)$, where k is the permeability, η is the viscosity of fluid, β is the compressibility of fluid and μ is the porosity of rock sample.

[46] In the experimental configuration adopted by *Brace and Martin* [1968], L_s is of the order of the sample length (38 mm). In contrast, in the present experimental configuration where a rock sample was inserted into a graphite sleeve, L_s is of the order of the sample radius (8 mm), because interstitial pores near the sample circumference surface are saturated with water during deformation. Hence, L_s in the present experiments is about one-fifth shorter than that in the experiments by *Brace and Martin* [1968]. In addition, η is smaller at a higher temperature ($\eta = 10 \times 10^{-4}$ Pa s at room temperature). Since most of the present experiments were conducted above 60°C, η ranges from 0.8×10^{-4} Pa s to 4×10^{-4} Pa s. The diffusion coefficient D will thus be about 2 to 10 times larger than that at room temperature. Further, the permeability of Tsukuba granite is around 5 times higher than that of Westerly granite as mentioned in section 2. These differences lead to a significant difference in the characteristic time t_c between the two; that is, t_c for the present experimental configuration is, at least, 1/300-fold shorter than that for the experimental configuration by *Brace and Martin* [1968]. It thus follows that the critical strain rate for the present experimental configuration is higher than 10^{-5}/s, and that the Tsukuba granite sample inserted into a graphite sleeve is permeable during the prefailure deformation at a strain rate of 10^{-5}/s.

[47] During the postfailure process, macroscopic failure surfaces are formed as a result of crack-crack interaction and coalescence, and the permeability necessarily increases. Note that the permeability is the lowest at an initial stage of nondeformed intact rock, and that it necessarily increases during the faulting process as a result of the growth of individual cracks, crack-crack interaction, and coalescence. This is clearly different from the deformation process of preexisting fault zone, where the permeability may decrease during the deformation as a result of the compaction of gouge particles. Indeed, it has been shown that the permeability of intact rock increases during the postfailure in the brittle regime [*Lockner et al.*, 2000].

[48] It is seen from Figure 9 that D_c increases with an increasing depth at depths greater than 10 km in both hydrostatic and suprahydrostatic pore pressure regimes, and that D_c is independent of P_c^{eff}. These indicate that the increase in D_c is not caused by dilatancy-hardening resulting from a change in P_c^{eff}, but by an increase in

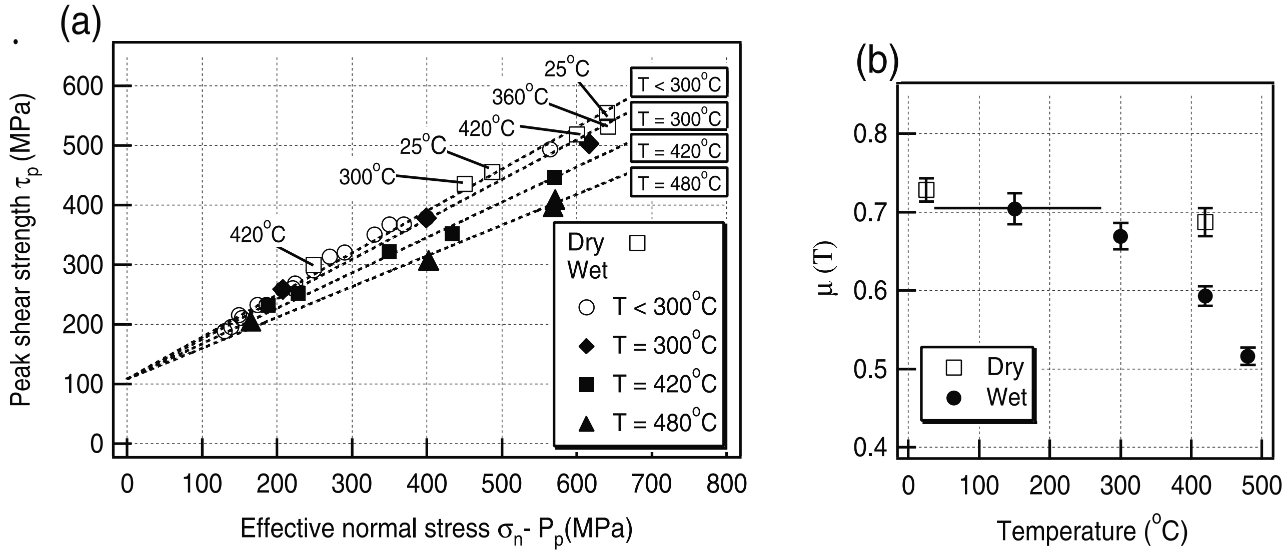

Figure 16. (a) A plot of the peak shear strength τ_p against the effective normal stress σ_n^{eff} (= $\sigma_n - P_p$). White circles, black diamonds, black squares and black triangles denote data on τ_p tested under wet conditions at temperatures below 300°C, at 300°C, 420°C, and 480°C, respectively. Broken lines denote the values of τ_p predicted by equation (9) under wet conditions. White squares represent data on τ_p tested under dry conditions at each temperature attached to the symbol. (b) A plot of $\mu(T)$ against temperature. Black circles and white squares show the values of $\mu(T)$ under wet and dry conditions. For details, see text.

temperature. This leads to the conclusion that the effective stress law holds in the postfailure process as well.

4.2. The Dependence of τ_p on Temperature and Effective Normal Stress

[49] To evaluate the peak shear fracture strength of intact rock portion (such as interlocking asperities) on a fault in seismogenic environments, we formulate τ_p of intact granite quantitatively as a function of the effective normal stress ($\sigma_n^{eff} = \sigma_n - P_p$) and temperature. Figure 16a shows a plot of τ_p against σ_n^{eff} for data in different ranges of temperature. We notice that τ_p below 300°C monotonically increases as a function of σ_n^{eff} under both wet and dry conditions, from which it is confirmed that τ_p is dependent on σ_n^{eff}, but is insensitive to temperature in the brittle regime. We also notice that τ_p above 300°C and at wet conditions is lower than that expected from the effect of σ_n^{eff} below 300°C, and that it becomes lower at higher temperatures. This indicates that τ_p is sensitive to both temperature and σ_n^{eff} above 300°C. Note, however, that τ_p at a dry condition and at temperatures higher than 300°C has almost the same value as that at wet conditions below 300°C. This suggests that τ_p at a dry condition is not significantly affected by temperature up to at least 420°C.

[50] The shear strength τ_p is in general a function of σ_n^{eff}, T and strain rate $\dot{\varepsilon}$. However, the effect of $\dot{\varepsilon}$ on τ_p on is beyond the scope of the present paper. We here assume that τ_p at a strain rate of 10^{-5}/s is expressed as a function of T and σ_n^{eff} by

$$\tau_p = C_o + \mu(T)\sigma_n^{eff}, \tag{9}$$

where C_o is the cohesive strength, and $\mu(T)$ is the internal frictional coefficient, which is assumed to be a function of T above 300°C. For data on τ_p below 300°C, an iterative least squares method was used to determine values for C_o and μ, and C_o = 108 ± 6 MPa and μ = 0.7 ± 0.02 were evaluated.

[51] It is clearly seen from Figure 16a that the rate of increase in τ_p against σ_n^{eff} becomes slower in wet environments as temperature increases above 300°C. This suggests that μ is temperature-dependent. We determine μ as a function of temperature using least squares fit by assuming that C_o is independent of temperature, and that C_0 = 108 MPa. The best-fitted value of $\mu(T)$ to the observed data set for wet conditions at each temperature is plotted in Figure 16b. It is found from Figure 16b that $\mu(T)$ at wet conditions decreases as temperature increases above 300°C. This suggests that the temperature range above 300°C for granite rock at wet conditions is in the brittle-plastic transition regime. By substituting the best-fitted value for $\mu(T)$ of equation (9), we have a specific relation between τ_p and σ_n^{eff} at each temperature, and broken lines in Figure 16a indicate those relations at different temperatures. Equation (9), where μ is assumed to be a function of temperature, well accounts for data on τ_p under wet conditions.

[52] On the other hand, it can be seen from Figure 16a that $\mu(T)$ for dry samples is almost independent of temperature, although the number of data tested under dry conditions is limited. This suggests that Tsukuba granite at a dry condition remains brittle in the temperature range up to 420°C (Figure 16b). The difference in $\mu(T)$ between at wet and dry conditions suggests that the weakening effect of water on τ_p is enhanced above 300°C.

[53] There is a vast difference in strain rate between rock deformation processes in the laboratory and in the field. Although it is well known that the effect of strain rate on τ_p in the brittle regime obeys a logarithmic law [e.g., *Masuda et al.*, 1987], its effect on τ_p in the brittle-plastic transition regime is still unclear, and a series of experiments is needed to reveal the strain rate effect in the brittle-plastic transition regime.

4.3. Implications

[54] It has been found from the present experiments that constitutive law parameters such as τ_p and D_c depend on both temperature and σ_n^{eff} above 300°C. As pointed out previously, this implies that the temperature range above 300°C for granite rock at wet conditions is in the brittle-plastic transition regime, which is indeed corroborated from the microscopic observation of the damage zone. It has been demonstrated that $|d\tau/dD|_{\max}$ ($\sim\Delta\tau_b/D_c$) decreases with increasing depth in a depth range from 10 to 15 km (Figure 11), where temperature is greater than 300°C. It has also been shown that G_c increases with increasing depth at depths greater than 10 km (Figure 12). In the brittle-plastic transition regime, G_c will partially include the work of plastic flow, which may contribute to an increase in G_c [*Scholz*, 1990]. These results indicate that the resistance to rupture growth increases at depths greater than 10 km, and that rupture instability is suppressed below the bottom of the seismogenic layer. This suppression of instability in the brittle-plastic transition regime is primarily responsible for the lower limit of seismicity and rupture zone of a large earthquake in the Earth's crust.

[55] Using focal mechanism solutions of microseismic events, *Iio* [1996] has reported that the onset of brittle-plastic transition in the Earth's crust coincides with the lower limit of seismicity. It has been pointed out by earlier authors [e.g., *Ito*, 1990] that the lower-limit of seismicity corresponds to the zone where temperature is higher than 300 ~ 400°C. These previous studies have discussed the lower-limit of seismicity in terms of the depth profile of shear resistance in the Earth's crust. However, the stability or instability of an earthquake rupture should be discussed in terms of the constitutive law for shear rupture, noting that the constitutive law is affected by seismogenic environments, which has been demonstrated in the present experiments.

[56] Note that $\Delta\tau_b \cong 100$ MPa for intact granite at depths shallower than 10 km (Figure 10) roughly coincides with the maximum breakdown stress drop estimated for earthquakes [e.g., *Ellsworth and Beroza*, 1995; *Bouchon*, 1997]. Such a high breakdown stress drop will be possible only when initially intact rock fails, because $\Delta\tau_b$ for intact rock gives the highest possible value of the breakdown stress drop for preexisting faults. In fact, there are increasing amounts of evidence that the distribution of $\Delta\tau_b$ on an earthquake fault is very heterogeneous. This strongly suggests that the earthquake rupture process that takes place at shallow crustal depths is a mixed process between frictional slip failure and the shear fracture of initially intact rock.

[57] It has been found from the present study that $\Delta\tau_b$ for intact granite has an almost constant value at depths, at least, shallower than 10 km. This is contrasted with the pervasive idea that $\Delta\tau_b$ increases with increasing depth in the brittle regime, and this pervasive idea is based on laboratory experiments on frictional slip failure on a precut fault. The fact that $\Delta\tau_b$ for intact granite has an almost constant value at shallow depths suggests that the upper limit of $\Delta\tau_b$ on a preexisting fault in the seismogenic layer is virtually constant irrespective of depth. This may be important when $\Delta\tau_b$ at a patch of high resistance to rupture growth (which may be called an asperity or barrier) on an earthquake fault is discussed. The present results will be significant and useful for more realistic simulation of the earthquake rupture process based on the constitutive law.

5. Conclusions

[58] Laboratory experiments have been performed to investigate how constitutive law parameters for the shear failure of intact Tsukuba granite are affected by seismogenic, wet environments. Tsukuba granite samples were deformed at the conditions simulating crustal depths ranging down to 15 km at a strain rate of 10^{-5}/s. Whether the effective stress law holds or not at the strain rate of 10^{-5}/s depends on the experimental configuration, and the law does hold at the strain rate of 10^{-5}/s in the present experimental configuration.

[59] The critical slip displacement D_c remains constant at simulated crustal depths shallower than 10 km; however, D_c increases with increasing depth at depths greater than 10 km. The increase in D_c at depths greater than 10 km is attributed to the effect of temperature in the brittle-plastic transition regime, which is attained above 300°C for granite rock deformed at a strain rate of 10^{-5}/s at wet conditions. The breakdown stress drop $\Delta\tau_b$ is roughly 100 MPa in a depth range down to 15 km, although there is a slight tendency for $\Delta\tau_b$ to decrease gradually with increasing depth in the hydrostatic pore pressure regime. It follows from these results that $|d\tau/dD|$ during the breakdown process decreases with increasing depth at depths greater than 10 km. The apparent fracture energy also increases with increasing depth at depths greater than 10 km. These results physically mean that the stability of the breakdown process is enhanced at depths greater than 10 km, due to the effect of temperature.

[60] At crustal depths shallower than around 10 km, the peak shear strength τ_p increases linearly with increasing depth; however, at depths greater than 10 km, it has a lower value than that extrapolated from the linear relation determined at the conditions of shallower depths. This suggests that the mechanical behavior of granite rock is semibrittle in a simulated depth range 10–15 km tested at wet conditions. This is corroborated from the microscopic observation of the fault zone: full plastic deformation for biotite, a little amount of plasticity for quartz, and no plasticity for feldspar. The microscopic observation also revealed that the width of cataclasite zone was in a range from 0.2 to 0.42 mm, and that the width of damage zone was roughly 1 mm. Since the widths of these zones are scale-dependent, the scaling law must be established, based on the underlying physics, to unify laboratory data with field data. This will be addressed in a future study.

[61] **Acknowledgments.** We would like to thank S. Yoshida for his thoughtful comments. Y. Takei and N. Shigematsu greatly helped us in microscopic observations of thin-sections. We are grateful to Associate Editor Karen Mair and two anonymous reviewers for their critical or constructive comments, which led to substantial improvement in the original manuscript.

References

Aki, K., Characterization of barriers on an earthquake fault, *J. Geophys. Res.*, *84*, 6140–6148, 1979.

Blanpied, M. L., D. A. Lockner, and J. D. Byerlee, Frictional slip of granite at hydrothermal conditions, *J. Geophys. Res.*, *100*, 13,045–13,064, 1995.

Bouchon, M., The state of stress on some faults of the San Andreas system as inferred from near-field strong motion data, *J. Geophys. Res.*, *102*, 11,731–11,744, 1997.

Brace, W. F., and R. J. Martin, A test of the law of effective stress for crystalline rocks of low porosity, *Int. J. Rock. Mech. Min. Sci.*, *5*, 415–426, 1968.

Byerlee, J. D., Friction, overpressure and fault normal compression, *Geophys. Res. Lett.*, *17*, 2109–2112, 1990.

Clauser, C., et al., thermal regime of the crystalline continental crust: Implications from KTB, *J. Geophys. Res.*, *102*, 18,417–18,441, 1997.

Crank, J., *The Mathematics of Diffusion*, 446 pp., Clarendon, Oxford, England, 1975.

Dieterich, J. H., Presesimic fault slip and earthquake prediction, *J. Geophys. Res.*, *83*, 3940–3948, 1978.

Ellsworth, W. L., and G. C. Beroza, Seismic evidence for an earthquake nucleation phase, *Science*, *268*, 851–855, 1995.

Fisher, A. T., G. Zwart, and Ocean Drilling Program Leg 156 Scientific Party, Relation between permeability and effective stress along a plate-boundary fault, Barbados accretionary complex, *Geology*, 307–311, 1996.

Hudson, J. A., S. L. Crouch, and C. Fairhurst, Soft, stiff and servocontrolled testing machines: A review with reference to rock failure, *Eng. Geol. Amsterdam*, *6*, 155–189, 1972.

Huenges, E., B. Engeser, J. Erzinger, W. Kessels, and J. Kuck, The permeable crust: Geohydraulic properties down to 9101m depth, *J. Geophys. Res.*, *102*, 18,255–18,265, 1997.

Ida, Y., Cohesive force across the tip of a longitudinal-shear crack and Griffith's specific surface energy, *J. Geophys. Res.*, *77*, 3796–3805, 1972.

Iio, Y., Depth-dependent change in the focal mechanism of shallow earthquakes: Implications for brittle-plastic transition in a seismogenic region, *J. Geophys. Res.*, *101*, 11,209–11,216, 1996.

Ito, K., Regional variations of the cutoff depth of seismicity in the crust and their relation to heat flow and large Inland-earthquakes, *J. Phys. Earth*, *38*, 223–250, 1990.

Jaeger, J. C., and N. G. W. Cook, *Fundamentals of Rock Mechanics*, 2nd ed., 585 pp., Chapman and Hall, New York, 1976.

Kanamori, H., The nature of seismic patterns before large earthquakes, in *Earthquake Prediction: An International Review*, edited by D. W. Simpson and P. G. Richards, pp.1–19, AGU, Washington, 1981.

Lockner, D. A., A generalized law for brittle deformation of Westerly granite, *J. Geophys. Res.*, *103*, 5107–5123, 1998.

Lockner, D. A., and J. D. Byerlee, Dilatancy in hydraulically isolated faults and the suppression of instability, *Geophys. Res. Lett.*, *21*, 2353–2356, 1994.

Lockner, D. A., J. D. Byerlee, V. Kuksenko, A. Ponomarev, and A. Sidorin, Quasi-static fault growth and shear fracture energy in granite, *Nature*, *350*, 39–42, 1991.

Lockner, D. A., H. Naka, H. Tanaka, H. Ito, and R. Ikeda, Permeability and strength of core samples from Nojima fault of the 1995 Kobe earthquake, *U.S. Geol. Surv. Open File Rep.*, *129*, 147–152, 2000.

Masuda, K., H. Mizutani, and I. Yamada, Experimental study of strain-rate dependence and pressure dependence of failure properties of granite, *J. Phys. Earth*, *35*, 37–66, 1987.

Matsu'ura, M., H. Kataoka, and B. Shibazaki, Slip-dependent friction law and nucleation processes in earthquake rupture, *Tectonophysics*, *211*, 135–148, 1992.

Moore, D. E., and D. A. Lockner, The role of microcracking in shear-fracture propagation in granite, *J. Struct. Geol.*, *17*, 95–114, 1995.

Moore, J. C., et al., Abnormal fluid pressures and fault-zone dilation in the Barbados accretionary prism: Evidence from logging while drilling, *Geology*, *23*, 605–608, 1995.

Morrow, C. A., Z. Chong, and J. D. Byerlee, Effective pressure law for permeability of Westerly granite under cyclic loading, *J. Geophys. Res.*, *91*, 3870–3876, 1986.

Odedra, A., M. Ohnaka, H. Mochiduki, and P. Sammonds, Temperature and pore water pressure effects on the shear strength of granite in the brittle-plastic transition regime, *Geophys. Res. Lett.*, *28*, 3011–3014, 2001.

Ohnaka, M., Earthquake source nucleation: A physical model for short-term precursors, *Tectonophysics*, *211*, 149–178, 1992.

Ohnaka, M., Nonuniformity of the constitutive law parameters for shear rupture and quasistatic nucleation to dynamic rupture: A physical model of earthquake generation processes, *Proc. Natl. Acad. Sci. U. S. A.*, *93*, 3795–3802, 1996.

Ohnaka, M., A physical scaling relation between the size of an earthquake and its nucleation zone size, *Pure Appl. Geophys.*, *157*, 2259–2282, 2000a.

Ohnaka, M., A constitutive scaling law that unifies the shear rupture from small scale in the laboratory to large scale in the earth as an earthquake source, paper presented at 2nd ACES Workshop, Tokyo and Hakone, Japan, 2000b.

Ohnaka, M., A constitutive scaling law and a unified comprehension for frictional slip failure, shear fracture of intact rock, and earthquake rupture, *J. Geophys. Res.*, *108*, doi:10.1029/2000JB000123, in press, 2003.

Ohnaka, M., and Y. Kuwahara, Characteristic features of local breakdown near crack-tip in the transition zone from skick-slip experiments to natural earthquakes, *Tectonophysics*, *175*, 197–220, 1990.

Ohnaka, M., and L.-F. Shen, Scaling of the shear rupture process from nucleation to dynamic propagation: Implications of geometric irregularity of the rupturing surfaces, *J. Geophys. Res.*, *104*, 817–844, 1999.

Ohnaka, M., and T. Yamashita, A cohesive zone model for dynamic shear faulting based on experimentally inferred constitutive relation and strong motion source parameters, *J. Geophys. Res.*, *94*, 4089–4104, 1989.

Ohnaka, M., Y. Kuwahara, and K. Yamamoto, Constitutive relations between dynamic physical paramerters near a tip of the propagating slip zone during stick-slip shear failure, *Tectonophysics*, *144*, 109–125, 1987.

Ohnaka, M., M. Akatsu, H. Mochizuki, A. Odera, F. Tagashira, and Y. Yamamoto, A constitutive law for the shear failure of rock under lithospheric conditions, *Tectonophysics*, *277*, 1–27, 1997.

Paterson, M. S., *Experimental Rock Deformation—The Brittle Field*, 254 pp., Springer-Verlag, New York, 1978.

Palmer, A. C., and J. R. Rice, The growth of slip surfaces in the progressive failure of over-consolidated clay, *Proc. R. Soc. London, Ser. A*, *332*, 527–548, 1973.

Press, W. H., S. A. Teukolsky, W. T. Vetterling, and B. P. Flannery, *Numerical Recipes in Fortran*, Cambridge Univ. Press, New York, 1992.

Reches, Z., and D. A. Lockner, Nucleation and growth of faults in brittle rocks, *J. Geophys. Res.*, *99*, 18,159–18,173, 1994.

Rice, J. R., Fault stress states, pore pressure distributions, and the weakness of the San Andreas Fault, in *Fault Mechanics and Transport Properties of Rock*, edited by B. Evans and T.-F. Wong, Academic, San Diego, Calif., 475–504, 1992.

Ruina, A. L., Slip instability and state variable friction laws, *J. Geophys. Res.*, *88*, 10,359–10,370, 1983.

Rummel, F. H., J. Alheid, and C. Frohn, Dilatancy and fracture-induced velocity changes in rock and their relation to frictional sliding, *Pure Appl. Geophys.*, *116*, 743–764, 1978.

Scholz, C. H., *The Mechanics of Earthquakes and Faulting*, 439 pp., Cambridge Univ. Press, New York, 1990.

Scholz, C. H., N. H. Dawers, J. Z. Yu, M. H. Anders, and P. A. Cowie, Fault growth and fault scaling laws: Preliminary result, *J. Geophys. Res.*, *98*, 21,951–21,961, 1993.

Sleep, N. H., Rate- and state-dependent friction of intact rock and gouge, *J. Geophys. Res.*, *104*, 17,847–17,856, 1999.

Vermilye, J. M., and C. H. Scholz, The process zone: A microstructual view of fault growth, *J. Geophys. Res.*, *103*, 12,223–12,237, 1998.

Wong, T.-F., Shear fracture energy of Westerly granite from post-failure behavior, *J. Geophys. Res.*, *87*, 990–1000, 1982.

Wong, T.-F., On the normal stress dependence of the shear fracture energy, in *Earthquake Source Mechanics*, *Geophys. Monograph Ser.*, vol. 37, edited by S. Das, J. Boatwright, and C. H. Scholz, pp. 1–11, AGU, Washington, D.C., 1986.

Yoshida, S., Convection current generated prior to rupture in saturated rocks, *J. Geophys. Res.*, *106*, 2103–2120, 2001.

Zoback, M. D., and H. P. Harjes, Injectio-induced earthquakes and crustal stress at 9 km depth at the KTB deep drilling site, Germany, *J. Geophys. Res.*, *102*, 18,477–18,491, 1997.

A. Kato, H. Mochizuki, and M. Ohnaka, Earthquake Prediction Research Center, Earthquake Research Institute, The University of Tokyo, Tokyo, Japan. (akato@eri.u-tokyo.ac.jp; u-mochi@eri.u-tokyo.ac.jp; ohnaka@fd.catv.ne.jp)